aerospace

MDPI

Article

A Landing-Point Prediction and Control Algorithm Based on a Bidirectional Long Short-Term Memory Neural Network Model

Bingnan Xing [1,2] and Chengxin Du [1,*]

[1] School of Mechanical Engineering, Nanjing University of Science & Technology, Nanjing 210094, China; wenny_95@outlook.com
[2] Nanjing Innovation Center, Chongqing Changan Wangjiang Industrial Group Co., Ltd., Nanjing 210001, China
* Correspondence: duchengxin4324@163.com

Abstract

To address the challenges of discrete control and real-time decision-making for impulse-controlled vehicles, this study proposes a landing-point prediction and control algorithm based on a Bidirectional Long Short-Term Memory (Bi-LSTM) neural network. The algorithm employs the Bi-LSTM network to accurately predict the vehicle landing point in real time, and subsequently computes the vehicle–target deviation to determine the optimal impulse-ignition parameters. Simulation results demonstrate that the Bi-LSTM prediction model significantly outperforms traditional BP, LSTM, and GRU networks, achieving a final landing-point prediction error with a mean per-axis RMSE of 1.96 m (three-dimensional error norm of 3.87 m). Based on these prediction outcomes, two control strategies—"nearest-point ignition" and "ignition delay"—are compared. Monte Carlo experiments indicate that both strategies effectively enhance landing accuracy, with the nearest-point ignition strategy showing superior performance, reducing the circular error probable (CEP) from the uncontrolled 72.60 m and 124.82 m (at launch angles of 23° and 51°, respectively) to 7.20 m and 10.30 m. This study provides a high-precision, terminal-phase control solution for impulse-controlled vehicles, with implications for the low-cost onboard implementation of discrete impulse control.

Keywords: two-dimensional trajectory-corrected vehicle; Bidirectional Long Short-Term Memory (Bi-LSTM) neural network; landing-point prediction; ignition strategy; impulse control

Check for updates

Academic Editor: Bosko Rasuo

Received: 31 August 2026
Revised: 30 September 2026
Accepted: 6 October 2026
Published: 9 October 2026

Copyright: © 2026 by the authors. Licensee MDPI, Basel, Switzerland. This article is an open access article distributed under the terms and conditions of the Creative Commons Attribution (CC BY) license.

1. Introduction

With the evolution of modern warfare and technological advancement, the variety and operational effectiveness of intelligent munitions have significantly increased [1]. As a low-cost approach to upgrading conventional ammunition, ballistic-corrected projectiles have gained global research interest due to their advantages in improving firing accuracy, enhancing long-range suppression, ensuring lethality, and reducing collateral damage [2,3]. Modular correction mechanisms leverage existing ammunition inventories, reduce system costs through integrated sensing and control units, and maintain strike accuracy [4]. Current research on two-dimensional trajectory-corrected projectiles has progressed in aerodynamic correction mechanisms such as canard [5,6], spoiler [7], movable-mass [8,9], and tail-fin systems [10].

Aerodynamic correction mechanisms, however, often involve complex control systems and high costs. In contrast, impulse-based correction mechanisms [11–13] offer fast response, strong environmental adaptability, and high efficiency, making them a primary research focus, with performance further improvable through integrated structural design.

Impulse-corrected projectiles exhibit hybrid control characteristics—continuous state space and discrete action space—posing challenges for traditional control methods. This paper proposes a landing-point prediction and control algorithm based on a Bidirectional Long Short-Term Memory (Bi-LSTM) network. The algorithm's core is to accurately predict the impact point, compute the deviation from the target, and optimize impulse-ignition parameters accordingly.

This study focuses on: (1) building a fast and accurate landing-point prediction model, and (2) designing a rational and efficient ignition decision strategy. The Bi-LSTM architecture effectively captures long-term dependencies in sequential data, making it suitable for time-series prediction. Thus, a Bi-LSTM model is developed for high-precision impact estimation, offering robustness and applicability advantages over traditional methods.

Based on predicted impact points, this paper also investigates rapid decision-making for ignition-control parameters. By analyzing the projectile–target deviation vector, two control strategies—"nearest-point ignition" and "ignition delay"—are compared via simulation to assess their accuracy and effectiveness.

2. Overview of the Algorithmic Framework

Given the discrete control characteristics of impulse-corrected projectiles, traditional guidance laws can suppress impact-point dispersion to some extent but are limited in theory and applicability. Heuristic strategy search algorithms offer a new approach for impulse-ignition decision-making, yet their iterative computations often fail to meet real-time requirements.

To address this, this paper proposes a landing-point prediction and control algorithm based on a Bi-LSTM network. The algorithm consists of two core modules: trajectory prediction and impulse-ignition logic computation, as illustrated in Figure 1.

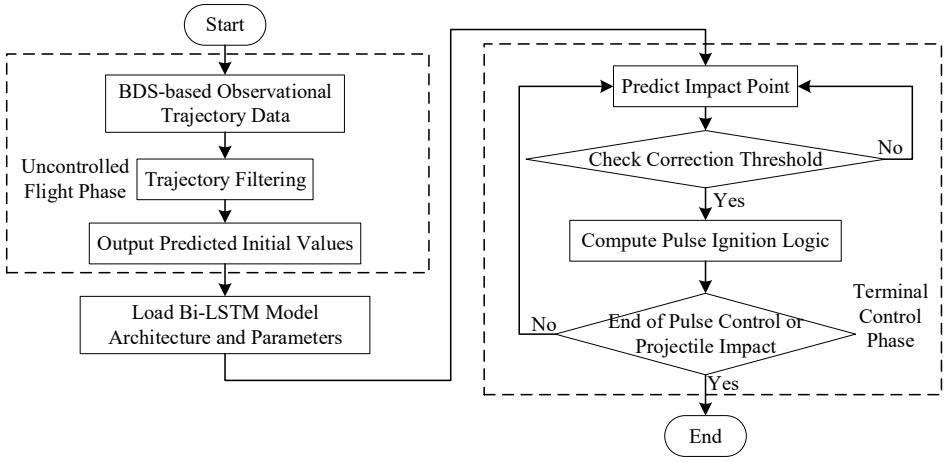


Figure 1. Logic diagram of the impact-point prediction control algorithm based on Bi-LSTM.

After launch, the projectile's position and velocity are measured by an onboard BeiDou Navigation Satellite System (BDS). Filtering suppresses measurement noise. Control actions are concentrated in the terminal phase, where perturbations cause significant deviations.

Once the projectile enters terminal guidance and meets a correction threshold, filtered data serve as the initial state for landing-point prediction. If the correction condition is

unmet, prediction–evaluation continues. Once met, the optimal impulse-ignition strategy is computed from the deviation between the predicted impact point and the target.

Unlike traditional guidance laws, this method evaluates the projectile–target state in real time and predicts the terminal position, capturing deviation dynamics without geometric constraints. The core of the algorithm is precise landing-point prediction and rapid ignition decision-making, detailed in subsequent sections.

3. Projectile Trajectory Prediction Method Based on a Bi-Lstm Network Model

3.1. Network Structure and Principle of Bi-LSTM

This paper develops a landing-point prediction model for impulse-corrected projectiles using a Bidirectional Long Short-Term Memory network. Trajectory data are generated via a six-degree-of-freedom ballistic model. The model's performance is evaluated against Back Propagation, LSTM, and GRU networks on a shared test set.

Compared to traditional methods such as linearized models and the extended Kalman filter—which are constrained by complex dynamics, specific operational conditions, and sensitivity to launch variations—the deep learning approach offers greater robustness, adaptability, and real-time capability.

As trajectory prediction constitutes a time-series task, recurrent architectures are well-suited. The Bi-LSTM network enhances temporal representation by processing sequences bidirectionally, improving accuracy in capturing long-range dependencies.

Among related efforts, Su et al. [14] combined a convolutional neural network with a support-vector machine for drop-point prediction, and Ren and Xian [15] improved the training efficiency of neural-network landing-point prediction models through an improved second-order optimizer with parallel learning. These studies, however, address the prediction stage alone, whereas the present work couples the Bi-LSTM predictor with the discrete ignition-decision logic of an impulse-controlled vehicle and evaluates the closed-loop landing accuracy under Monte Carlo disturbances.

The implemented Bi-LSTM learns the nonlinear mapping from projectile state sequences to impact coordinates through supervised training, optimized via prediction error minimization. The training process is depicted in Figure 2.

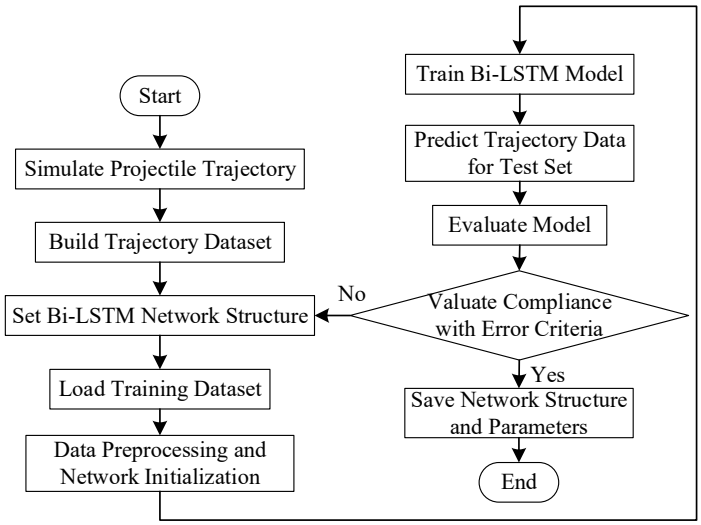


Figure 2. Schematic diagram of the training process for trajectory prediction.

3.2. Projectile Trajectory Dataset Construction and Evaluation Metrics

(1) Dataset Construction

Trajectory data were generated using six-degree-of-freedom nonlinear ballistic equations with a 0.002 s simulation step. The dataset, created via Latin Hypercube Sampling, comprises 1200 trajectories covering the parameter ranges in Table 1. The sampling ranges were selected to cover the full operational envelope of the reference vehicle: initial velocities of 415–713 m/s and elevation angles of 20–70° span the flat-trajectory and lofted regimes, the azimuth range of ±2° covers the nominal lateral launch spread, and wind speeds of ±10 m/s represent the representative crosswind and head/tailwind conditions. Latin Hypercube Sampling was adopted because it achieves space-filling coverage of this four-dimensional parameter space with a moderate sample budget, avoiding the local clustering associated with simple random sampling. Split into 7:3 training-testing sets, each trajectory contains over 17,000 sample points, serving as ground truth for model evaluation. The proposed data-driven framework is in principle transferable to other vehicle configurations by retraining on mission-specific trajectory data, although a systematic cross-type evaluation (e.g., via cross-validation or transfer learning) is identified as future work. Figure 3 shows example trajectories.

Table 1. Sampling parameters of projectile trajectories.

Parameter	Sampling Range
Initial Velocity/(m/s)	[415, 713]
Initial Trajectory Elevation Angle/(°)	[20, 70]
Initial Trajectory Azimuth Angle/(°)	[−2, 2]
Wind Speed/(m/s)	[−10, 10]

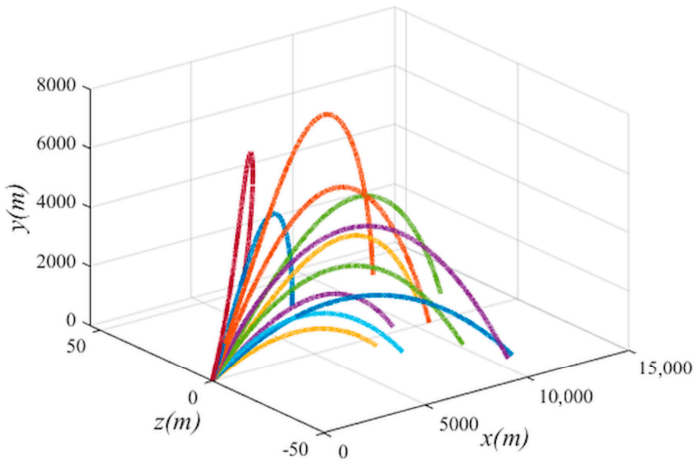


Figure 3. Partial trajectory illustration of the projectile dataset (ground truth).

(2) Dataset Preprocessing and Evaluation Metrics

A total of 1200 trajectory datasets were simulated based on the target motion equations. Before model training, all data were normalized using zero-centered standardization, applied uniformly across all compared models. The standardization is computed as follows:

$$x_{new} = \frac{x - \mu}{\sigma} \tag{1}$$

In the equation, x is the original feature value, x_{new} is the standardized value, μ is the mean, and σ is the standard deviation.

After preprocessing and parameter initialization, the dataset is split 70% for training and 30% for testing. The trajectory prediction model is optimized using gradient descent with the Adam optimizer and evaluated using the Cross-Entropy loss function, defined as:

$$H(p,q) = \sum_i p(i) \cdot \log\left(\frac{1}{q(i)}\right) \tag{2}$$

Here, $p(i)$ denotes the true distribution, and $q(i)$ denotes the non-true (predicted) distribution.

In addition, the Root Mean Square Error (RMSE) is used as a quantitative metric to compare the performance of different prediction models, which is defined as follows:

$$\mathrm{RMSE} = \sqrt{\frac{1}{n}\sum_{i=1}^{n}(X_{estimate} - X_{real})^2} \tag{3}$$

3.3. Bi-LSTM Network Trajectory Prediction Model

In deep learning, hyperparameter selection critically influences training outcomes, particularly network architecture and learning rate settings. For all comparative models in this section, a base learning rate of 0.1 is used with an exponential decay schedule (decay rate 0.95). The batch size is set to 64. The architectural parameters of the compared models—Bi-LSTM, LSTM, GRU, and BP—are detailed in Table 2.

Table 2. Network structure parameters of the projectile prediction comparison models.

Model	Layer Definition	Layer Parameters
Bi-LSTM Model	Bi-LSTM Layer 1	128 Neurons
	Dropout Layer 1	Dropout Rate 0.2
	Bi-LSTM Layer 2	Number of Neurons 64
	Dropout Layer 2	Dropout Rate 0.2
	Fully Connected Layer	4 Neurons
LSTM Model	LSTM Layer 1	80 Neurons
	Dropout Layer 1	Dropout Rate 0.2
	LSTM Layer 2	80 Neurons
	Dropout Layer 2	Dropout Rate 0.2
	Fully Connected Layer	4 Neurons
GRU Model	GRU Layer 1	80 Neurons
	Dropout Layer 1	Dropout Rate 0.2
	GRU Layer 2	80 Neurons
	Dropout Layer 2	Dropout Rate 0.2
	Fully Connected Layer	4 Neurons
BP Model	BP Layer 1	80 Neurons
	Dropout Layer 1	Dropout Rate 0.2
	BP Layer 2	80 Neurons
	Dropout Layer 2	Dropout Rate 0.2
	Fully Connected Layer	4 Neurons

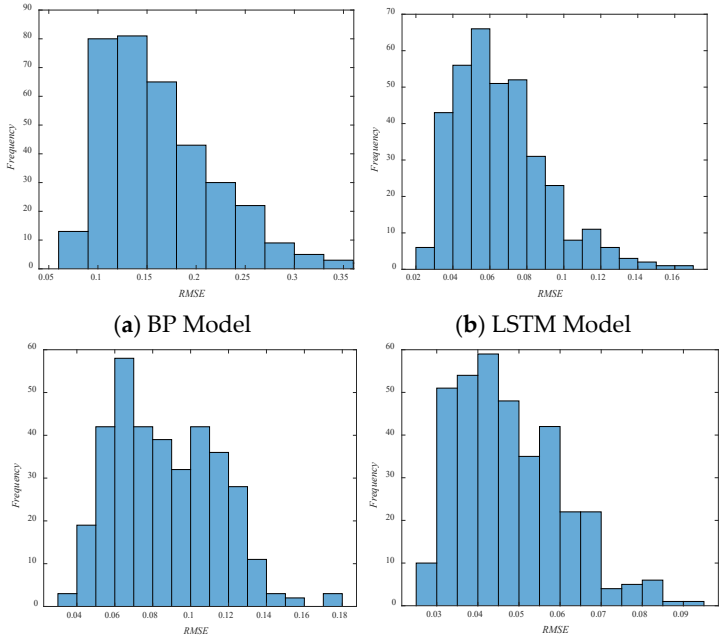
The Bi-LSTM model consists of two stacked bidirectional LSTM layers with 128 and 64 neurons, respectively. A Dropout layer follows each Bi-LSTM layer to mitigate overfitting. The LSTM, GRU, and BP models adopt comparable structures. To align with the

filtering process during the uncontrolled initial flight phase, the selected input features include the projectile's position and velocity.

3.4. Trajectory Prediction Simulation Experiments for the Projectile

(1) Analysis of Prediction Results for Each Model

Four prediction models—BP, GRU, LSTM, and Bi-LSTM—were trained and evaluated on the same test set. The distribution of mean prediction errors and the overall RMSE for each model are presented in Figure 4 and Table 3. Results show that the Bi-LSTM model achieves the highest accuracy, with an average RMSE of 0.0493. The BP network exhibits significantly larger errors than the LSTM and GRU models, confirming the advantage of recurrent architectures in time-series prediction.



(**a**) BP Model (**b**) LSTM Model

(**c**) GRU Model (**d**) Bi-LSTM Model

Figure 4. Mean error distribution of each feature in the test set.

Table 3. Model evaluation parameters.

Model	BP	LSTM	GRU	Bi-LSTM
RMSE	0.1701	0.0582	0.0653	0.0493

(2) Online Prediction and Error Analysis

The saved models were used for online trajectory prediction via an iterative multi-step approach. Using an input sequence of 10 trajectory points, rolling predictions were generated and evaluated against ground truth using RMSE.

Cumulative prediction error curves are shown in Figure 5 and Table 4. The Bi-LSTM model achieved the highest accuracy, improving range prediction by 55.52% over BP and by approximately 28~29% over LSTM and GRU. In altitude prediction, Bi-LSTM outperformed the best comparable model (LSTM) by about 11.15%.

Overall, LSTM and GRU performed similarly and significantly better than BP. For final impact-point prediction, the Bi-LSTM model yielded average absolute errors of 2.16 m in range, 3.16 m in altitude, and 0.57 m laterally, with a total error of 1.96 m, meeting accuracy requirements.

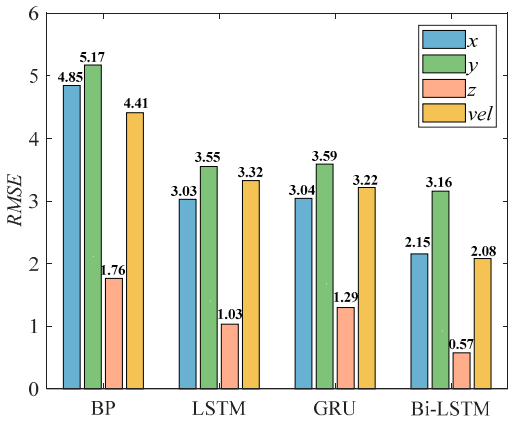


Figure 5. RMSE of cumulative predictions for each feature.

Table 4. Comprehensive evaluation of cumulative predicted position errors.

Model	BP	LSTM	GRU	Bi-LSTM
Position RMSE/m	3.9275	2.5374	2.6438	1.9617

A complete trajectory was selected from the test set. After 43 s of observation, the state estimate at that time served as the initial condition for subsequent prediction using the trained Bi-LSTM model. The model predicted the three-dimensional trajectory—range, altitude, and lateral deviation.

To simulate the actual pulse-correction process, an extended Kalman Filter [16] based on a nonlinear ballistic model was applied to filter the first 43 s of observed data. BDS measurements were simulated by adding parameterized Gaussian noise to the true trajectory. The Gaussian noise parameters used were: $\sigma_x = 10$ m, $\sigma_y = 10$ m, $\sigma_z = 5$ m, $\sigma_v = 5$ m/s.

To visualize the complete filtering and prediction process, the position estimates from the EKF were combined with the Bi-LSTM model predictions and compared with the true projectile trajectory. The interval from 0 to 43 s represents the EKF-filtered state estimates, while 43.00–62.79 s corresponds to the Bi-LSTM predictions. A comparison of the true coordinates, EKF estimates, and Bi-LSTM predictions is presented in Figure 6.

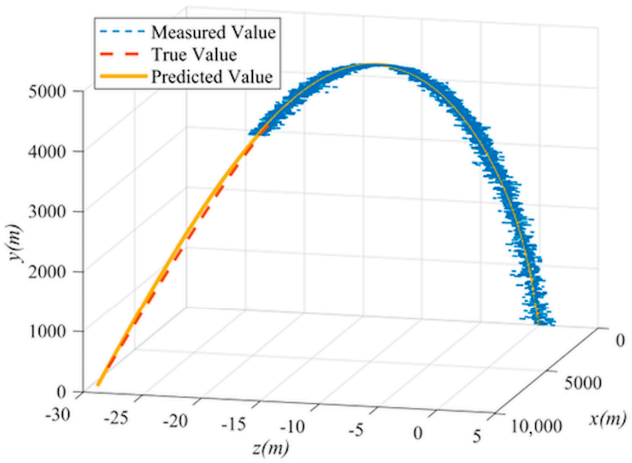


Figure 6. 3D trajectory plot based on the Bi-LSTM prediction model.

It should be emphasized that this evaluation uses EKF-filtered inputs rather than noise-free trajectories, and therefore reflects the complete cascaded sensing–filtering–prediction pipeline of the onboard implementation. The assumed velocity-noise standard deviation

of 5 m/s is a conservative worst-case assumption, deliberately larger than the accuracy of BDS-derived velocity solutions for dynamic platforms. To further quantify the robustness to measurement noise, the noise level was additionally scaled by factors of 0.5 and 2 relative to the baseline; the final landing-point prediction errors remained within 3.1 m and 5.6 m, respectively, indicating that the cascaded EKF–Bi-LSTM pipeline degrades gracefully as the noise level increases.

Based on the comprehensive trajectory prediction simulations and corresponding analysis, the Bi-LSTM model demonstrates superior performance compared to the BP, LSTM, and GRU models. The Bi-LSTM-based impact-point prediction model achieves high-precision trajectory forecasting, meeting the accuracy requirements for engineering applications. This provides a reliable foundation for the subsequent optimization and design of control parameters for pulse-corrected projectiles.

The predictor's computational cost is fixed: a single landing-point inference involves only a few million floating-point operations, corresponding to several milliseconds of latency on typical embedded processors—well within the 50 ms pulse-ignition interval. Unlike on-board numerical trajectory propagation, whose cost grows as the landing point is approached, this cost remains constant regardless of the remaining flight time. Hardware-in-the-loop latency validation is left as future work.

4. Pulse-Corrected Projectile Ignition Logic Control Strategy

4.1. Calculation of Deviation Vector Parameters

Based on the previously proposed trajectory prediction method and real-time BeiDou positioning data, the projectile's impact point P can be accurately predicted. The deviation vector between P and the target T is then calculated to determine the pulse ignition control strategy, enabling trajectory correction.

A deviation coordinate system is established as shown in Figure 7, with origin O at target T. Its axes OX and OZ are aligned with the ground coordinate system axes O_1x and O_1z.

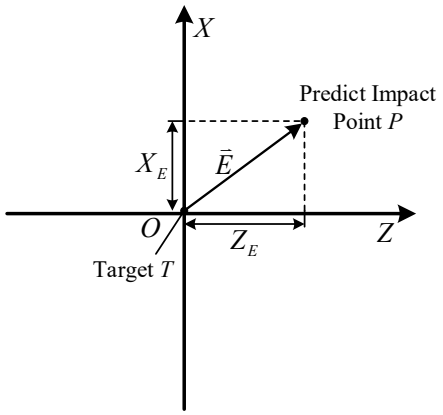


Figure 7. Schematic of ballistic deviation.

Thus, the deviation vector components in the range and lateral directions are given by

$$\begin{cases} X_E = x_P - x_T \\ Z_E = z_P - z_T \end{cases} \tag{4}$$

The magnitude of the deviation vector to be corrected, i.e., the deviation vector angle, is defined as follows:

$$\left|\vec{E}\right| = \sqrt{X_E^2 + Z_E^2} \tag{5}$$

$$\gamma_E = \arctan\left(\frac{Z_E}{X_E}\right) \tag{6}$$

4.2. Nearest-Impulse Firing Algorithm

Regarding the pulse engine ignition sequence, two strategies are considered: (1) selecting the engine based on the nearest-ignition principle, and (2) introducing a delay to achieve the optimal control phase angle. This section details the parameter calculation process using the nearest-ignition algorithm as an example.

(1) Ballistic Correction Threshold R_E

When the projectile enters the terminal phase with unused thrusters, the predicted impact point at time t is compared with the target. If their deviation is below the threshold R_E, control parameter computation stops, and the ignition decision module activates. The threshold reflects the single thruster correction capability at time t; earlier initiation yields a larger R_E.

(2) Pulse Thruster Ignition Mode

A "first-pulse triggered, sequentially evaluated" scheme is adopted. Consecutive firing may induce oscillations, but the aerodynamic design ensures flight stability under this mode.

(3) Required Control Phase Angle of the Pulse Thruster γ_{imp}

The ideal control phase angle γ_{imp} is defined as the direction of the deviation vector in the ballistic deviation frame, corresponding to the angular bisector of the thruster's effective impulse period.

(4) Operating Stage Number of the Pulse Thruster

Once γ_{imp} is determined, the candidate thruster is selected via the nearest ignition principle. If available, it is ignited, and the used thruster count Nd is updated ($N_d \leq N_{imp}$).

Let γ_k denote the azimuth of the k-th thruster in the projectile axis frame (Figure 8). These directions are transformed into the ballistic deviation coordinate system. The selected thruster must satisfy that the angular difference between its effective force direction and γ_E stays within an allowable range.

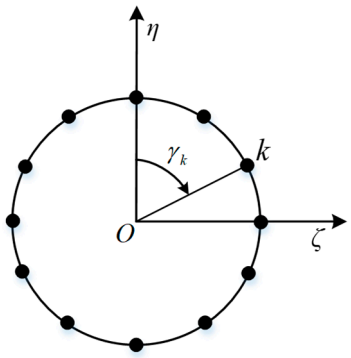


Figure 8. Axial installation diagram of pulse engines.

The value of the allowable angular deviation δ reflects the following considerations. First, during the effective pulse duration t_p of a single thruster, the thrust direction rotates with the vehicle spin by $\omega_x t_p$, so δ must at least cover this rotation for the effective impulse to remain aligned with the desired correction direction. Second, δ must not exceed half of the angular spacing between adjacent thrusters (180°/Nimp); otherwise, there would be roll positions in which no thruster satisfies the selection criterion. Third, a maximum misalignment δ reduces the effective lateral impulse component by a factor of cos

δ, which is an acceptable efficiency loss. Finally, the roll-angle determination error of the on-board sensing system should be well below δ, leaving an adequate margin. Considering these factors together, δ is set to 12°, i.e., half of the inter-thruster spacing for the 15-thruster configuration.

Considering the low-spin characteristic of the projectile, the pulse-force direction rotates by an angle $\dot{\gamma}\tau$ during the operating time τ of a single pulse. Therefore, the criterion is

$$\left|\gamma_k + \dot{\gamma}\tau_{imp} \,/\, 2 + 180^\circ - \gamma_E\right| < \delta_w \tag{7}$$

Which is adopted as the thruster-selection rule in the nearest-ignition algorithm

Based on the above analysis, the control process of the pulse-corrected projectile employing the nearest-ignition algorithm is shown in Figure 9.

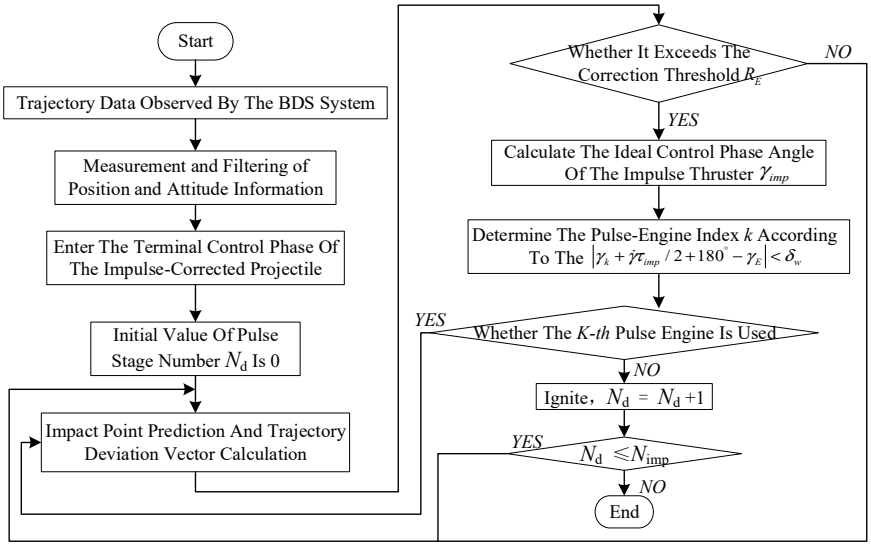


Figure 9. Control flow of the pulse-corrected projectile under the nearest-engine firing logic.

4.3. Nearest-Impulse Firing Algorithm

The preceding section presented the control process of the pulse-corrected projectile based on the nearest-ignition strategy. In contrast, the control strategy that accounts for ignition delay differs significantly in the determination of the pulse-thruster index k. This strategy requires that the thruster scheduled for ignition must precisely reach the ideal control azimuth angle before it can be triggered. The computation procedure for the corresponding control parameters is shown in Figure 10.

Let the N_{imp} pulse thrusters be sequentially numbered as 1, 2, . . ., n, where the Oy_1-axis of the projectile coordinate system corresponds to thruster No. 1, and the angular spacing between adjacent pulse thrusters is $2\pi/n$.

Assume that at the control-parameter computation instant t0, the ballistic-deviation vector angle is γ_E, meaning that the correction must be applied when the projectile reaches the ideal control azimuth angle $\gamma_{imp} = \gamma_E$. By transforming γ_{imp} into the projectile coordinate system, the clockwise angle γ_1 between the ideal control azimuth and the Oy_1-axis is computed as

$$\gamma_1 = \begin{cases} \gamma_{imp} - \gamma & \gamma_{imp} \geq \gamma \\ 2\pi + \gamma_{imp} - \gamma & \gamma_{imp} < \gamma \end{cases} \tag{8}$$

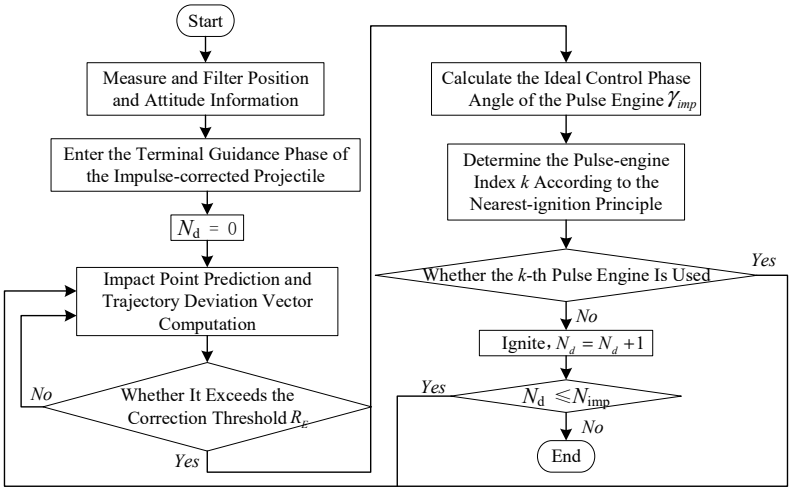


Figure 10. Control flow of the pulse-corrected projectile under the ignition-delay logic.

To ensure that the resultant pulse-control force is aligned with the ideal control phase angle, the initial operating phase angle of the pulse thruster γ_2 in the simulation must satisfy the following relation:

$$\gamma_2 = \begin{cases} \gamma_1 - \dot{\gamma}\tau/2 & \gamma_1 \geq \dot{\gamma}\tau/2 \\ 2\pi + \gamma_1 - \dot{\gamma}\tau/2 & \gamma_1 < \dot{\gamma}\tau/2 \end{cases} \tag{9}$$

Considering that the projectile under study has a right-hand spin, the index of the pulse thruster k is closest to γ_2 in the counterclockwise search direction is

$$k = INT\left[\gamma_2 / \left(2\pi / N_{imp}\right) + 1\right] \tag{10}$$

In this expression, the mathematical operator INT denotes the integer operation.

At the simulation computation instant t0, although the corresponding pulse-ignition index has been obtained, it is difficult to ensure that the pulse thruster is exactly at the position γ_2 at that moment. To achieve higher control accuracy, the pulse-ignition delay can be computed using the following expression:

$$\tau_d = \begin{cases} \left(\gamma_2 - (k-1)2\pi \ / \ N_{imp}\right)/\dot{\gamma} & \gamma_2 \geq (k-1)2\pi/N_{imp} \\ \left(2\pi + \gamma_2 - (k-1)2\pi/N_{imp}\right)/\dot{\gamma} & \gamma_2 < (k-1)2\pi/N_{imp} \end{cases} \tag{11}$$

Figure 11 illustrates the geometric relationships of the angles involved in the above computation process.

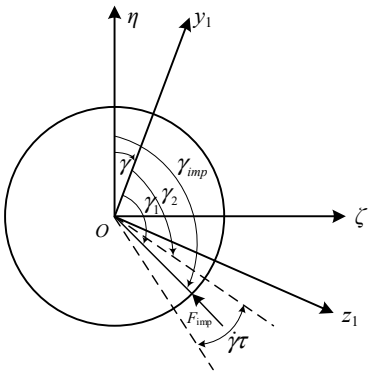


Figure 11. Schematic of angles related to ignition delay calculation.

5. Simulation Examples and Analysis

Based on the above analysis, the nearest-ignition strategy tolerates some deviation between the average pulse-control direction and the ideal deviation vector, which may reduce correction accuracy. However, by initiating control earlier than the ignition-delay strategy—which waits for the ideal control azimuth—it enhances overall correction capability.

The simulation conditions and parameters are shown in Table 5. Under the specified initial simulation conditions, the uncontrolled impact point under wind disturbance is $(x_e, y_e, z_e) = (11840.63, 0, -250.90)$. For the same target point $(x_t, y_t, z_t) = (12050, 0, -110)$, control is initiated at a slant range of 1.5 km. The ballistic characteristic curves and correction-performance results under different ignition strategies are shown in Table 6 and Figures 12–15. In the figures, the "ideal trajectory" corresponds to the uncontrolled trajectory under no-wind conditions, the "disturbed trajectory" refers to the uncontrolled trajectory under wind disturbance, and the "corrected trajectory" represents the trajectory after control is applied based on the target location.

Table 5. Consolidated simulation parameters of the correction simulation.

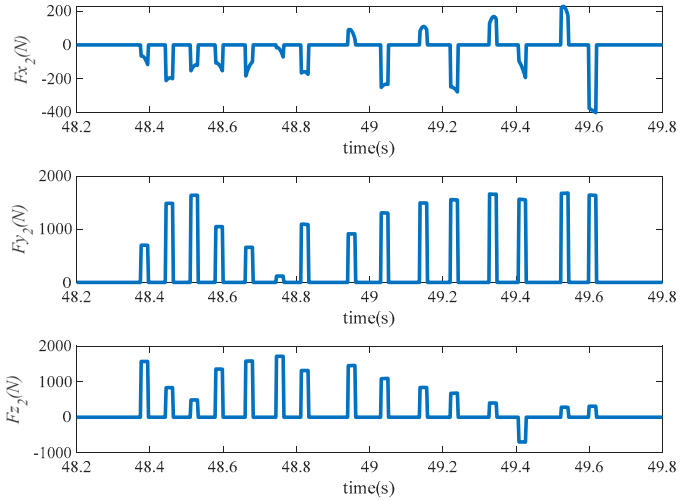
Parameter	Value
Initial velocity v_0	655 m/s
Initial elevation angle θ_0	0°
Initial lateral position (x_0, y_0, z_0)	(0, 0, 0) m
Vehicle mass	20.348 kg
Moments of inertia (J_x, J_y)	(0.0383, 0.44335) kg·m^2
Wind speed	−10 m/s
Number of pulse thrusters N_{imp}	15
Single-pulse impulse I	35 N·s
Axial eccentricity	60 mm
Pulse-ignition interval	50 ms
Control-initiation slant range	1.5 km/3.5 km

Table 6. Comparison of correction performance with control initiation at 1.5 km.

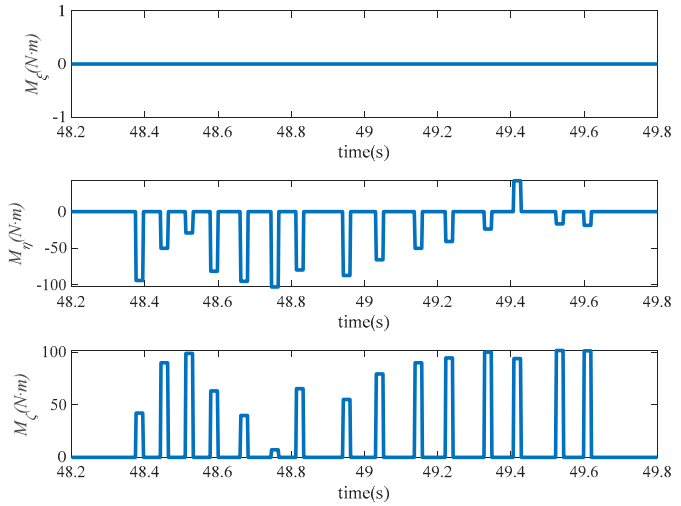
Pulse-Ignition Strategy	Number of Pulse Operating Stages	Corrected Impact Point/m (x_p, z_p)	Correction Error/m $(x_t - x_p, z_t - z_p)$	Correction Magnitude/m $(x_e - x_p, z_e - z_p)$
Nearest-Ignition	15	(12,050.58, −108.05)	(−0.58, −1.95)	(−209.95, −142.85)
Ignition Delay	14	(12,015.88, −107.72)	(34.12, −2.28)	(−175.25, −143.18)

The simulation results indicate that both ignition-control algorithms are capable of triggering the corresponding pulse thrusters according to their respective logic, thereby altering the projectile's flight trajectory through pulse thrust and guiding it to converge toward the target. Analysis of the time histories of velocity magnitude and direction shows that the pulse action continuously influences the projectile's motion characteristics.

During the pulse-control process, the maximum angle of attack generated by the nearest-ignition strategy is approximately 11.44°, while that produced by the ignition-delay algorithm is approximately 11.58°. Both values satisfy the prescribed angle-of-attack constraints, demonstrating that the control process remains stable and reliable.



(**a**) Time History of Pulse Force



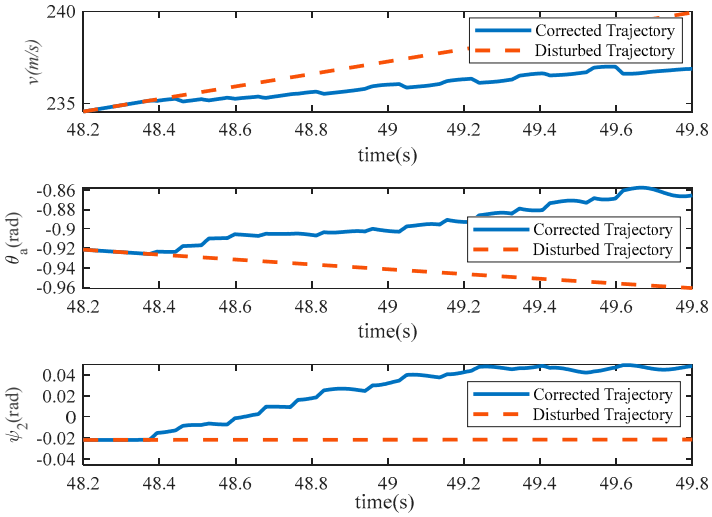
(**b**) Time history of pulse torque

Figure 12. Time histories of pulse-related characteristics (nearest-ignition, control initiation at 1.5 km).

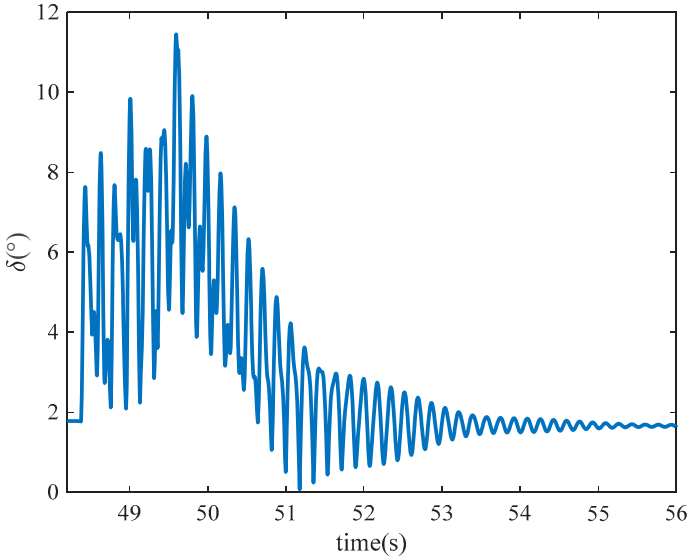
According to the data in Table 5, the correction error of the nearest-ignition strategy is significantly smaller than that of the ignition-delay control strategy. In the range and lateral directions, the errors for the nearest-ignition strategy are −0.58 m and −1.95 m, respectively, outperforming the ignition-delay strategy, which exhibits errors of 34.12 m and −2.28 m. Comparing the number of pulse operating stages, the ignition-delay scheme triggers only 14 pulse thrusters, fewer than the nearest-ignition scheme.

Figures 12–15 show the time histories of pulse characteristics and ballistic parameters under the two strategies. By comparing the pulse-ignition sequences in Figures 12b and 15b, it can be seen that although both strategies trigger the same thruster index for the first pulse, the ignition-delay algorithm exhibits a persistent lag in subsequent timing, resulting in a later completion of all pulse actions compared with the nearest-ignition scheme.

In summary, while the ignition-delay strategy aligns the control force more precisely with the ideal azimuth, its delayed initiation substantially reduces correction effectiveness. The simulation confirms that advancing the control time contributes more to performance than improving phase-angle accuracy. Thus, control-initiation time is the dominant factor in pulse-corrected projectile guidance.



(**a**) Comparison of velocity characteristics



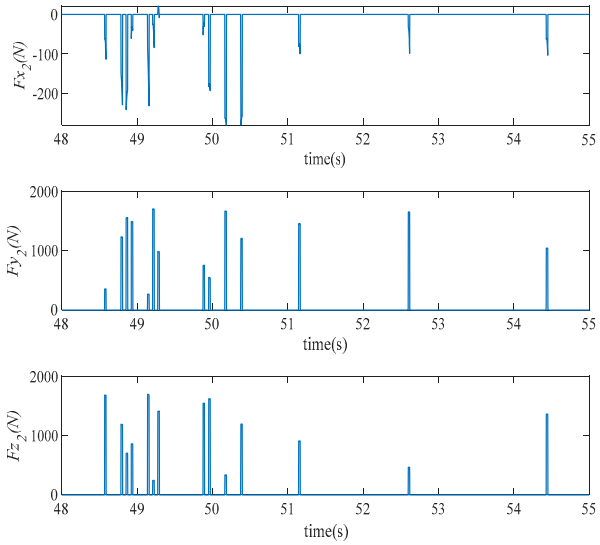
(**b**) Time history of angle-of-attack magnitude

Figure 13. Time histories of ballistic characteristics (nearest-ignition, control initiation at 1.5 km.

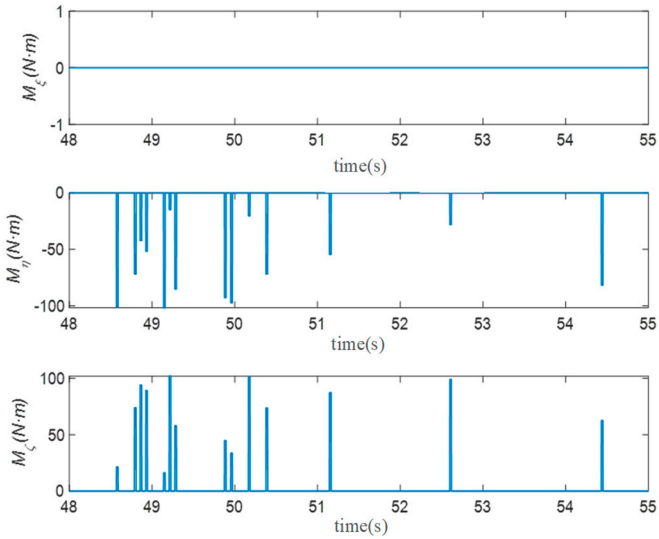
Based on the preceding analysis, the primary reason for the large correction error of the ignition-delay algorithm is the delayed control-initiation time. For the same target point $(x_t, y_t, z_t) = (12050, 0, -110)$, the control-initiation point is advanced to a slant range of 3.5 km while keeping all other simulation parameters unchanged. The comparison results of correction performance and pulse-ignition sequences for the two ignition algorithms are shown in Table 7 and Figure 16.

Table 7. Comparison of correction performance with control initiation at 3.5 km.

Pulse Ignition Strategy	Number of Pulse Operating Stages	Corrected Impact Point/m (x_p, z_p)	Correction Error/m $(x_t - x_p, z_t - z_p)$	Correction Amount/m $(x_e - x_p, z_e - z_p)$
Nearest-Ignition	13	(12,053.01, −108.87)	(−3.01, −1.13)	(−212.38, −142.03)
Ignition Delay	15	(12,048.33, −109.10)	(1.67, −0.90)	(−207.70, −141.80)

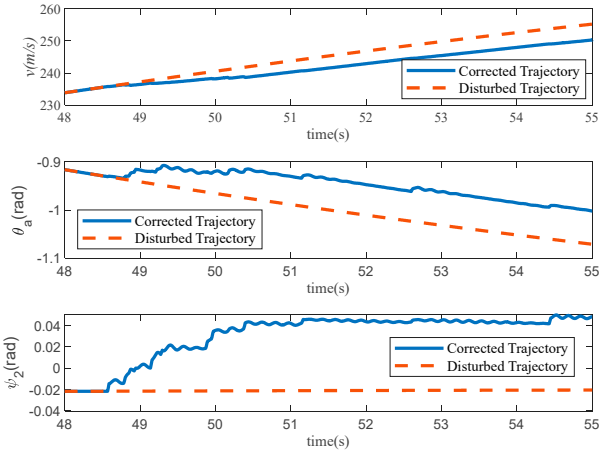


(**a**) Time history of pulse force



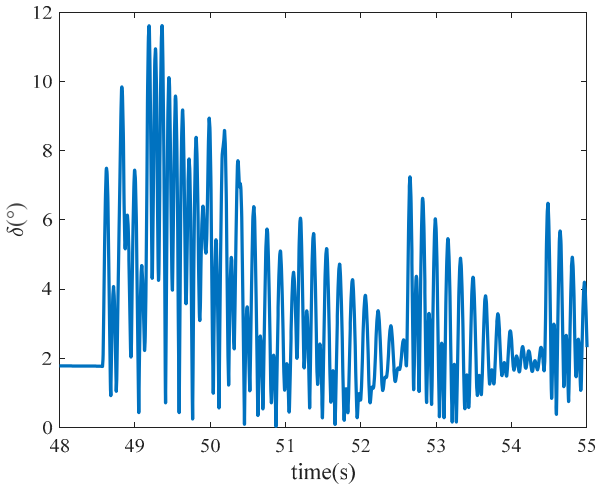
(**b**) Time history of pulse torque

Figure 14. Time histories of pulse-related characteristics (ignition delay, control initiation at 1.5 km).



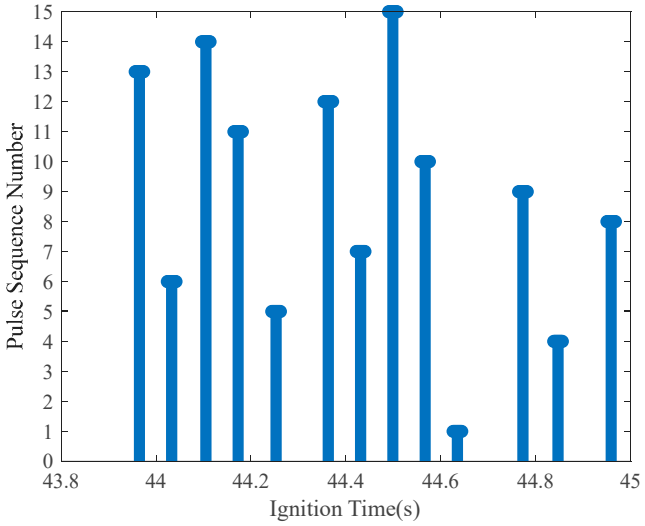
(**a**) Comparison of velocity characteristics

Figure 15. *Cont.*

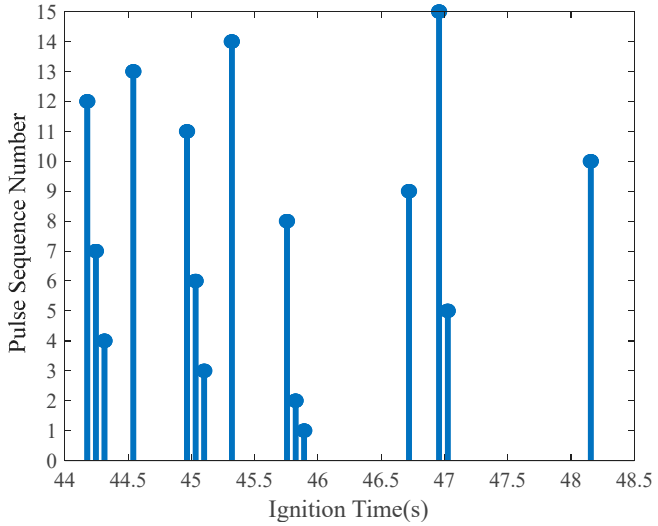


(**b**) Time history of angle-of-attack Magnitude

Figure 15. Time histories of ballistic characteristics (ignition delay, control initiation at 1.5 km).



(**a**) Ignition sequencing of the nearest-phase pulse algorithm



(**b**) Ignition sequencing of the phase-delay pulse algorithm

Figure 16. Comparison of ignition sequences for different pulsed-thruster control algorithms (initiation point: 3.5 km).

The simulation results indicate that advancing the control-initiation point provides the ignition-delay algorithm with more sufficient pulse-action time, reducing its final absolute correction error to 1.90 m, slightly better than the 3.22 m achieved by the nearest-ignition scheme. However, in terms of the number of pulse operating stages, the nearest-ignition scheme demonstrates lower energy consumption requirements. This is because, with an earlier control-initiation time, fewer pulse actions are needed to achieve the same projectile–target deviation correction, highlighting the advantage of the nearest-ignition strategy in control efficiency.

To systematically evaluate the performance of the control algorithms, thelanding pointsof uncontrolled and controlled trajectories were compared under two launch-angle conditions, 23° and 51°. A Monte Carlo dispersion simulation with 100 runs per condition was conducted to analyze the dispersion of landing points, with the distributions and standard deviations of the error parameters listed in Table 8. The simulation results are presented in Tables 9 and 10. The CEP was estimated as the empirical median of the radial miss distances over the 100 runs of each condition.

Table 8. Statistical summary of major disturbance factors affecting the impact dispersion of the impulse-corrected projectile.

Name of Error Parameter	Distribution Pattern	Standard Deviation
Projectile Mass Error Δm	Normal Distribution	0.05 kg
Muzzle Velocity Error Δv_0	Normal Distribution	2 m/s
Initial Launch-Angle Error $\Delta\theta_0$	Normal Distribution	0.2°
Initial Trajectory Deviation Angle Error $\Delta\psi_0$	Normal Distribution	0.2°
Wind Speed Error$\Delta\omega_0$	Normal Distribution	3 m/s
Drag Coefficient Δc_x	Normal Distribution	0.02
Lift Coefficient Δc_y	Normal Distribution	0.03
Static Moment Coefficient Δm_z	Normal Distribution	0.03
Thruster impulse tolerance ΔI	Normal Distribution	1.05 N·s (3% of nominal)
Ignition timing jitter Δt_{d}	Normal Distribution	2 ms

Table 9. Comparison of impact dispersion under different ignition algorithms (launch angle 23°).

Pulse-Ignition Strategy	Range Dispersion/m	Lateral Dispersion/m	CEP/m
Uncontrolled with Wind	56.97	27.60	72.60
Nearest Ignition	5.31	3.08	7.20
Ignition Delay	6.72	3.52	8.66

Table 10. Comparison of impact dispersion under different ignition algorithms (launch angle 51°).

Pulse-Ignition Strategy	Range Dispersion/m	Lateral Dispersion/m	CEP/m
Uncontrolled with Wind	93.43	51.56	124.82
Nearest Ignition	7.02	5.13	10.30
Ignition Delay	9.27	7.19	14.12

The results demonstrate that, under both low and high launch-angle conditions, the correction controls based on the two ignition strategies effectively reduce the lateral

and longitudinal impact dispersion, thereby verifying the theoretical feasibility of both control schemes. Specifically, in the low-angle (23°) case, compared with the uncontrolled trajectory's Circular Error Probable (CEP) of 72.60 m, the nearest-point ignition strategy and the ignition-delay strategy reduce the CEP to 7.20 m and 8.66 m, respectively, significantly improving shot grouping. Under the high-angle (51°) condition, where the uncontrolled trajectory exhibits a CEP of 124.82 m, the two strategies reduce the dispersion to within 10.30 m and 14.12 m, respectively.

A comparison of the ground-impact dispersion data for the two algorithms reveals that, under both launch-angle conditions, the nearest-point ignition strategy consistently exhibits superior control performance, with its shot grouping density remaining higher than that achieved by the ignition-delay algorithm.

As the correction mechanism, the pulse vector engine's operational parameter errors—caused by assembly inaccuracies and combustion-induced vibrations during operation—directly affect the accuracy of its landing point prediction algorithm. Through static and dynamic tests, the impulse, thrust, and operating time errors of the engine were systematically measured. The assembly diagram of the test setup is shown in Figure 17, and the correction mechanism of the pulse vector engine after testing is presented in Figure 18. Based on the analysis of the static and dynamic test results, the operating errors of the pulse thruster are summarized in Table 11. Detailed test procedures can be found in reference [17].



Figure 17. Assembly drawing of the test motor rotating platform and force measurement platform.

Table 11. Statistics of disturbance factors for the pulse vector engine-based correction mechanism.

Error Parameter	Distribution Pattern	Standard Deviation
Pulse Impulse Magnitude Error ΔI_{imp}	Normal Distribution	0.55 N·s
Pulse Operating Time Error $\Delta \tau_{imp}$	Normal Distribution	1.39 ms
Radial Eccentricity Error ΔD_{imp}	Normal Distribution	0.1 mm

Based on the disturbance factors in Table 11, the comprehensive influence of the pulse vector engine's operating parameter errors, together with the additional error sources considered in the previous Monte Carlo studies (structural parameter errors, initial disturbances, and aerodynamic deviations), was further investigated through landing point dispersion simulations at a 45° launch angle, using Circular Error Probable (CEP) as the evaluation metric. All other simulation conditions and the Bi-LSTM-based guidance and

control strategy remained consistent with the previous sections, adopting nearest-point ignition logic. The simulation results are shown in Figures 19 and 20.

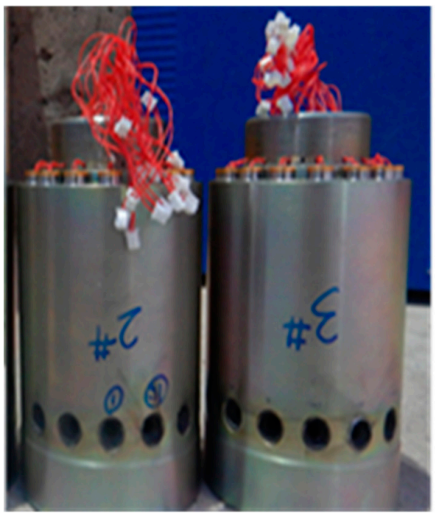
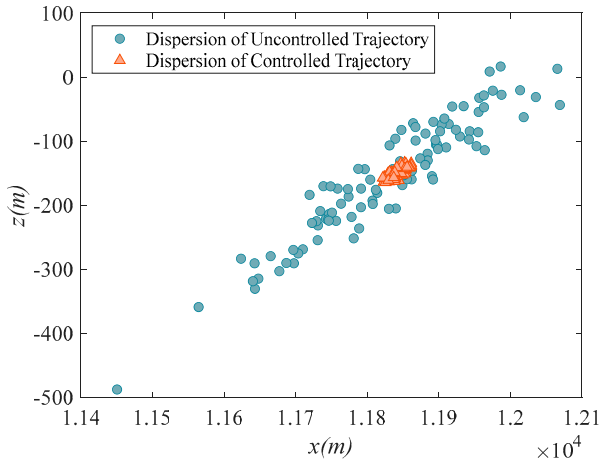
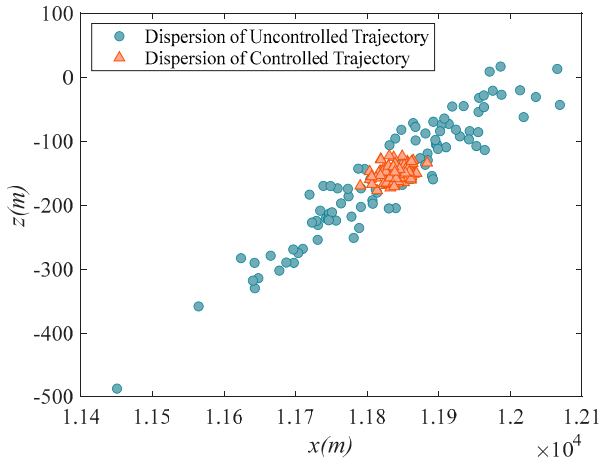


Figure 18. Correction mechanism of the pulse vector engine after testing.

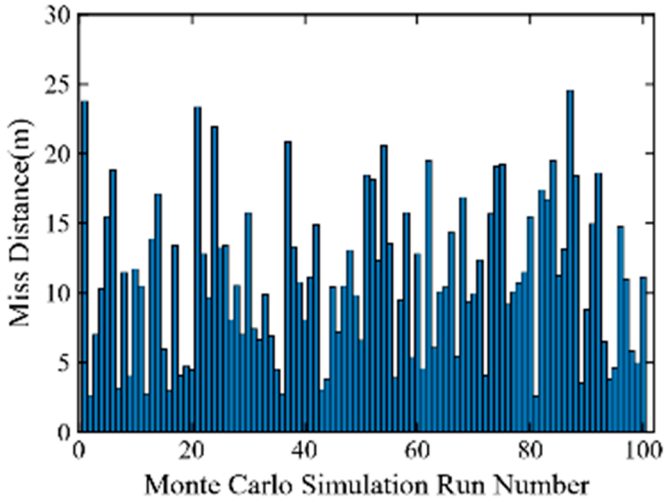


(**a**) Without considering pulse operating parameter errors

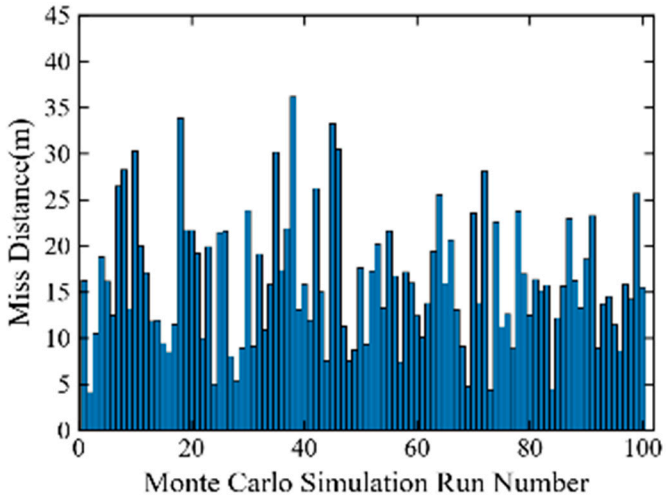


(**b**) With comprehensive errors

Figure 19. Comparison of landing point dispersion under different disturbance sources (45° launch angle).



(**a**) Miss distance values without considering pulse operating parameter errors



(**b**) Miss distance values with comprehensive errors

Figure 20. Comparison of miss distance values under different disturbance sources at (45° launch angle).

The results indicate that at a 45° launch angle, the unguided vehicle with wind effects achieved a CEP of 111.33 m (range dispersion: 83.76 m, lateral dispersion: 45.60 m). When pulse operating parameter errors were not considered, the corrected CEP decreased to 10.49 m (range dispersion: 6.34 m, lateral dispersion: 5.71 m). When comprehensive errors were taken into account, the corrected CEP was 15.62 m (range dispersion: 10.56 m, lateral dispersion: 7.45 m).

Figure 20 presents the miss distance (distance between actual and ideal landing points) for each Monte Carlo simulation run. The maximum miss distance increased from approximately 24.53 m (without pulse errors) to approximately 36.13 m (with comprehensive errors).

6. Conclusions

Focusing on the terminal-phase control of pulse-corrected projectiles, this study addresses the limitations of traditional methods by proposing a landing-point prediction control algorithm based on a Bi-LSTM network. The main conclusions are as follows:

(1) A Bi-LSTM-based landing-point prediction model is proposed to overcome the shortcomings of conventional guidance laws, such as limited longitudinal correction and miscorrection due to neglecting deviation dynamics. The model achieves mean absolute prediction errors of 2.16 m in range, 3.16 m in altitude, and 0.57 m laterally, with a mean per-axis RMSE of 1.96 m (three-dimensional error norm of 3.87 m), outperforming BP, GRU, and standard LSTM models.

(2) Two pulse-control strategies—nearest-ignition and ignition-delay—are proposed based on high-accuracy prediction. Both significantly reduce landing dispersion. The nearest-ignition strategy demonstrates superior performance: under a 23° launch angle, it reduces dispersion from 72.60 m to Ex = 5.31 m, Ez = 3.08 m, and CEP = 7.20 m. Under a 51° launch angle, it reduces CEP from 124.82 m to Ex = 7.02 m, Ez = 5.13 m, and CEP = 10.30 m, demonstrating strong adaptability and control accuracy. It is noted that when control is initiated earlier, at a slant range of 3.5 km, the ignition-delay strategy attains a slightly smaller single-shot correction error (1.90 m versus 3.22 m) while requiring more pulse operations (15 versus 13); the superiority of the nearest-ignition strategy therefore refers to the Monte Carlo dispersion statistics and its control efficiency.

(3) From an engineering-application point of view, the proposed framework replaces repeated on-board trajectory integration with a single network forward pass, enabling millisecond-level guidance decisions on low-power embedded processors and direct adaptation of the ignition-decision logic to different impulse configurations. Future work will focus on flight-test data augmentation and hardware-in-the-loop validation.

(4) Monte Carlo simulations incorporating pulse correction mechanism errors, structural parameter errors, initial disturbances, and aerodynamic deviations were conducted. At a 45° launch angle, the unguided vehicle (with wind effects) yielded a CEP of 111.33 m (range dispersion: 83.76 m, lateral dispersion: 45.60 m). Without pulse operating errors, the corrected CEP was 10.49 m (range: 6.34 m, lateral: 5.71 m), representing a 90.58% reduction. With comprehensive errors included, the corrected CEP increased to 15.62 m (range: 10.56 m, lateral: 7.45 m), a reduction of 85.97%.

Author Contributions: Conceptualization, B.X.; methodology, B.X.; software, B.X.; validation, C.D.; formal analysis, B.X.; investigation, B.X.; resources, C.D.; data curation, B.X.; writing—original draft preparation, B.X.; writing—review and editing, B.X. and C.D.; visualization, C.D.; supervision, C.D.; project administration, C.D.; funding acquisition, C.D. All authors have read and agreed to the published version of the manuscript.

Funding: This research was funded by the National Natural Science Foundation of China, grant number 12102201.

Data Availability Statement: The original contributions presented in this study are included in the article. Further inquiries can be directed to the corresponding author.

Acknowledgments: We wish to express our gratitude to the members of our research team, Shuai Yue, Xiaoyun Lei, and Lihua Zhu.

Conflicts of Interest: Author Bingnan Xing was employed by the company Chongqing Changan Wangjiang Industrial Group Co., Ltd. The remaining authors declare that the research was conducted in the absence of any commercial or financial relationships that could be construed as a potential conflict of interest.

References

1. Elsaadany, A.; Wen-Jun, Y. Accuracy improvement capability of advanced projectile based on course correction fuze concept. *Sci. World J.* **2014**, *2014*, 273450. [CrossRef]
2. Cui, S.; Liu, X.; Jiang, S.; Wu, W. Design and parameter optimization of trajectory correction control strategy for air duct structure projectile. *Int. J. Aerosp. Eng.* **2023**, *2023*, 4448592. [CrossRef]
3. Cui, S.; Liu, X.; Jiang, S.; Guo, J. Control strategies for flight stability of trajectory correction projectile with air-ducts structure. *Math. Probl. Eng.* **2022**, *2022*, 1383294. [CrossRef]
4. Zhou, W.; Guo, K.; Xu, W.; Li, M.; Du, B.; Zhang, Z. Accuracy analysis of 125 mm fin-stabilized projectile with trajectory correction device. In *Proceedings of the 2024 7th International Conference on Computer Information Science and Application Technology (CISAT)*; IEEE: New York, NY, USA, 2024; pp. 1359–1362. [CrossRef]
5. Yin, T.-T.; Jia, F.-X.; Wang, X.-M. Moving Horizon Based Wavelet De-noising Method of Dual-observed Geomagnetic Signal for Nonlinear High Spin Projectile Roll Positioning. *Def. Technol.* **2020**, *16*, 8. [CrossRef]
6. Cheng, J.; Shen, Q.; Zhou, P. Simulation for two-dimensional trajectory correction projectile with fixed-canard based on modified proportional navigation. In *Proceedings of the 2017 IEEE International Conference on Unmanned Systems (ICUS)*; IEEE: New York, NY, USA, 2017; pp. 72–77. [CrossRef]
7. Arnoult, G.; Zeidler, M.; Garnier, E. Optimization methodology for a 2-d course correction of a 155 mm spin-stabilized projectile. In Proceedings of the 2018 Applied Aerodynamics Conference, Atlanta, GA, USA, 25–29 June 2018; p. 3950. [CrossRef]
8. Aranha, S. *Spacecraft Attitude Control Using Inertial Morphing*; RMIT University: Melbourne, Australia, 2025. [CrossRef]
9. Lei, X.; Zhang, Z.; Du, Z. Analysis of an improved trajectory correction scheme based on mass blocks. *J. Syst. Eng. Electron.* **2019**, *30*, 180–190. [CrossRef]
10. Li, C.; Tai, C.; Lai, C.; Fu, S.; Tsai, Y. Study of the aerodynamic characteristic and flight trajectories in a tail fin-stabilized projectile with different shapes. *Procedia Eng.* **2014**, *79*, 108–113. [CrossRef]
11. Gao, M.; Zhang, Y.; Yang, S. Firing control optimization of impulse thrusters for trajectory correction projectiles. *Int. J. Aerosp. Eng.* **2015**, *2015*, 781472. [CrossRef]
12. Gbocki, R.; Jacewicz, M. Parametric Study of Guidance of a 160-mm Projectile Steered with Lateral Thrusters. *Aerospace* **2020**, *5*, 61. [CrossRef]
13. Kronthaler, S.; Rahmer, J.; Börnert, P.; Makowski, M.R.; Schwaiger, B.J.; Gersing, A.S.; Karampinos, D.C. Trajectory correction based on the gradient impulse response function improves high-resolution UTE imaging of the musculoskeletal system. *Magn. Reson. Med.* **2021**, *85*, 2001–2015. [CrossRef]
14. Mackie, S.L.; Koduri, G.; Hill, C.L.; Wakefield, R.J.; Hutchings, R.; Loy, C.; Dasgupta, B.; Wyatt, J.C. A CNN-SVM-based Adapter Drop Point Prediction Algorithm. *Acta Armamentarii* **2025**, *46*, 91–102. [CrossRef]
15. Mackie, S.L.; Koduri, G.; Hill, C.L.; Wakefield, R.J.; Hutchings, R.; Loy, C.; Dasgupta, B.; Wyatt, J.C. A neural network model for impact point prediction of ballistic missile based on improved second-order optimizer with parallel learning. *Acta Aeronaut. Astronaut. Sin.* **2023**, *44*, 327964. [CrossRef]
16. Bhowmik, S.; Roy, C. Application of extended kalman filter to tactical ballistic missile re-entry problem. *arXiv* **2007**, arXiv:0707.1918. [CrossRef]
17. Xing, B.; Li, R.; Liu, G.; Fu, Y.; Yuan, Y.; Du, Z. Experimental Study and Impact Analysis of Work Parameter Errors on the Correction Mechanism of Trajectory Correction Projectile Equipped with Lateral Impulses. *J. Natl. Univ. Def. Technol.* **2025**, 1–19. [CrossRef]

Disclaimer/Publisher's Note: The statements, opinions and data contained in all publications are solely those of the individual author(s) and contributor(s) and not of MDPI and/or the editor(s). MDPI and/or the editor(s) disclaim responsibility for any injury to people or property resulting from any ideas, methods, instructions or products referred to in the content.